Optics Letters

Simultaneous dual-channel stimulated Raman scattering microscopy demultiplexed at distinct modulation frequencies

Sandro Heuke, Barbara Sarri, Xavier Audier, and Hervé Rigneault*

Aix Marseille Univ, CNRS, Centrale Marseille, Institut Fresnel, Marseille, France
**Corresponding author: herve.rigneault@fresnel.fr*

Received 15 May 2018; revised 21 June 2018; accepted 25 June 2018; posted 26 June 2018 (Doc. ID 331728); published 23 July 2018

To increase the information per pixel in stimulated Raman scattering (SRS) microscopy as well as to correct from artifacts, it is valuable to acquire images at two different Raman shifts. We present a three-color SRS approach acquiring two perfectly registered SRS images where both pump beams are modulated at distinct frequencies while demodulating the Stokes beam. Our implementation uses two optical parametric oscillators that can be tuned to an almost arbitrary energy difference of Raman shifts, allowing investigation of fingerprint resonances simultaneously to CH-stretch vibrations.

OCIS codes: (180.4315) Nonlinear microscopy; (290.5910) Scattering, stimulated Raman; (170.6935) Tissue characterization.

https://doi.org/10.1364/OL.43.003582

Stimulated Raman scattering (SRS) is a versatile tool for fast, label-free, low-background imaging of molecular bonds present in biological samples [1]. Recent publications demonstrated its utility in particular for diagnostic purposes by generation of virtual-haematoxylin-and-eosin (H&E) stained images [2,3]. The reported implementations require at least two images acquired at two distinct Raman shifts, which may be obtained by fast tuning of the laser source [4]. The latter is still time-consuming as every sample area has to be imaged twice. Furthermore, the sequential registration of images is at risk in fresh samples that can move while drying or be distorted during the measurement procedure.

To overcome this drawback or to remove the background from SRS images arising from thermal lensing or cross-phase modulation [5] multiple methods were developed to allow for simultaneous detection of SRS images at distinct Raman shifts. SRS techniques investigating two or more Raman resonances simultaneously may be grouped [1] into (1) femtosecond-pulse, (2) chirped-pulse, and (3) modulation-multiplexed approaches. The former (1) uses a broadband femtosecond laser in combination with a grating after the sample to separate colors of the femtosecond pulse that are detected by a multi-element detector and demodulated numerically [6] or a multi-channel lock-in amplifier [7]. As the major disadvantage, strong scattering samples may lead to non-negligible crosstalk between channels that can be overcome by replacing the spectrometer by a Fourier-transform detection scheme at the price of a slower image acquisition [8]. Alternatively, Zhang *et al.* presented a combination of a femtosecond-laser system with an angle-to-wavelength pulse shaper composed of a grating and an acousto-optic modulator (AOM) [9]. The latter is used to shift the incident angle of the illumination of the grating while changing the wavelength after a following aperture. As the major disadvantage power is lost generating narrow-band picosecond pulse out of a femtosecond laser.

The second approach (2) implements spectral focusing [10] at two different time delays to address different Raman frequencies [11]. Detection of the signal is performed by a single lock-in detector at 90° phase difference. The method's scalability is limited to two colors, but can be extended if—instead of a dual-phase multiplexing scheme—a fast delay line is used that results in a quasi-simultaneous image acquisition [12,13]. Still, extra power is deposed onto the sample without further signal generation as a consequence of the only partial temporal interaction of the pump and Stokes pulse.

The third approach (3) utilizes an acousto-optical tunable filter (AOTF) to modulate different colors of a femtosecond-Ti:Sapphire laser output at different modulation frequencies while a second narrow-band beam is modulated at 20 MHz [14]. The signal is demodulated by a lock-in amplifier and further postprocessed *in silico* using the Fourier spectrum to assign individual contributions from different Raman resonances. The AOTF modulation range, however, is restricted to 200 kHz limiting the pixel dwell times to tens of microseconds. As an alternative, spatial frequency multiplexing is used instead of an AOTF to modulate the amplitude of one broadband beam at up to 3 MHz [15]. Yet, all methods presented share the limitation of a narrow spectral range of accessible Raman bands that is frequently centered around the CH-stretching vibrations. We present here a new approach enabling two arbitrary narrow vibrational frequency bands to be probed simultaneously. The proposed scheme uses a three-color picosecond laser system of which two are modulated at different frequencies in the megahertz range. The third color is detected by a single photo-diode (PD) and demodulated using two separate lock-in

amplifiers. As an advantage over previous implementations, the full relevant Raman spectral range, i.e., 500–5000 cm^{-1}, can be accessed while no laser power is wasted changing the pulse length nor do scattering compromise the signal quality. Furthermore, tuning both pump beams to match the CH-stretching vibrations at 2850 cm^{-1} and 2930 cm^{-1} allows for the generation of perfectly coregistered virtual-H&E images [2] as the vantage point for further manual or automated prediction of diagnosis [16].

The implementation of the dual-color SRS scheme requires only a minor alteration of the previous published setup [17,18]. Briefly, a Yb-fiber laser (APE Emerald engine, 2–3 ps, 80 MHz) pumps two optical parametric oscillators (OPO APE Emerald) at the second harmonic of 1031 nm (see Fig. 1). The latter is used directly as Stokes to drive the SRS process. The emission of the OPO signals used as pump beams can be tuned independently over the full spectral range from 680–980 nm to match molecular vibrations from 500 cm^{-1} to 5000 cm^{-1}. Both OPO outputs are separately guided through and modulated by AOMs (AA, MT200-B100A0,5-800) at distinct frequencies up to 25 MHz.

All three wavelengths are spatially and temporally superimposed by means of two dichroics and delay stages. The joined beams are coupled into a home-built laser scanning SRS microscope. A 20× objective (Nikon, CFI PLAN APO LBDA, NA = 0.75, immersion:air) or 40× objective (Nikon, PLAN, NA = 1.15, immersion:water) is used to focus the beams onto the sample. At the sample plane the power is approximately 20 mW for each beam. The stimulated Raman gain signal experienced by the Stokes beam (1031 nm) is collected in the forward direction using a 60× objective (Nikon, Fluor, NA = 1, immersion:water). Using suitable dielectric filters, the pump beams are blocked while the Stokes is centered onto a PD (APE SRS photodiode). The latter is connected to two independent lock-in amplifiers (APE) to demodulate the signal at the individual modulation frequencies of the pump beams. The modulation and signal extraction scheme is visualized in Fig. 2. The OPO pump wavelengths 1 and 2 are modulated at frequency f_1 and f_2, respectively, resulting in a modulation of the Stokes power at both frequencies that are readily separable by a power spectrum analyzer or lock-in amplifier. Note that the excess noise of the Yb-fiber laser—the major source of noise of the experimental configuration—was measured to be 10 dB(W) ≈ 3 dB(V), i.e., the image quality in Figs. 3 and 4 may be obtained within 1/10 of the acquisition time using a purely shot noise limited system. As an example, the performance of the dual-color implementation is highlighted in Fig. 3. Here, SRS images are displayed of a polystyrene (PS) bead's aromatic stretching vibration at 3050 cm^{-1} [19] as well as a gel of retinol containing retinol crystals at the fingerprint-resonance at 1590 cm^{-1} corresponding to the C = C stretching vibrations [20]. The OPO1 and OPO2 pump wavelengths were tuned to 784.4 nm and 884.3 nm while the modulation frequencies were set to $f_1 = 17.5$ MHz and $f_2 = 20.0$ MHz, respectively. Clearly, it can be observed that Fig. 3(a) reveals only the morphology of the PS beads, which are partially enclosed by the retinol gel. In turn,

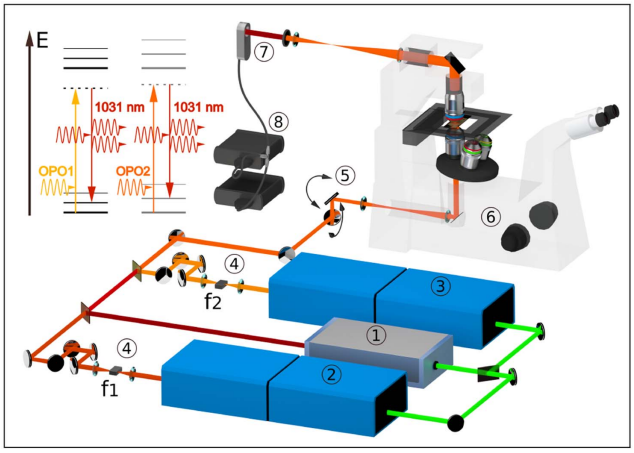

Fig. 1. SRS-energy diagrams and experimental setup: (1) Yb-fiber laser, (2) OPO1, (3) OPO2, (4) AOM, (5) laser scanning mirrors, (6) laser-scanning microscope, (7) PD, (8) lock-in amplifier.

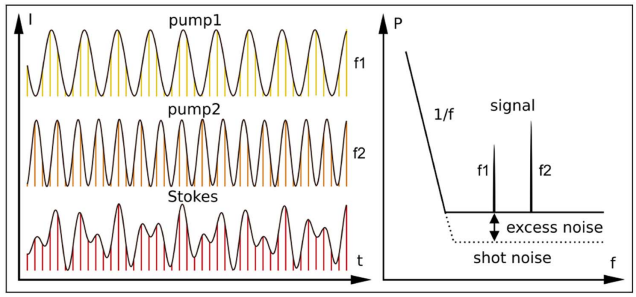

Fig. 2. Modulation scheme and power spectrum: the sinusoidal intensity modulation of the two pump beams is imprinted on the Stokes beam intensity after interaction with the sample. The power spectrum of the Stokes beam displays peaks at the modulation frequencies of the pump beams as a result of stimulated Raman gain (SRG).

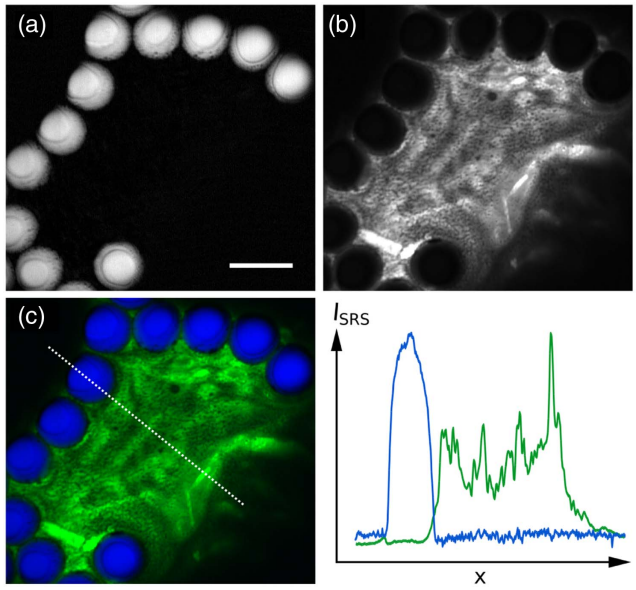

Fig. 3. Dual-color SRS images: (a) PS beads at 3050 cm^{-1} (false color: blue), (b) retinol gel distribution at 1590 cm^{-1} (false color: green). (c) Composite image of (a) and (b) as well as the SRS intensity profile along the dotted line. Scale bar equals 40 µm. Image parameters: pixel dwell time = 40 µs, $f_1 = 17.5$ MHz, $f_2 = 20.0$ MHz, resolution = 1800 × 1600, total image acquisition time: 26 s.

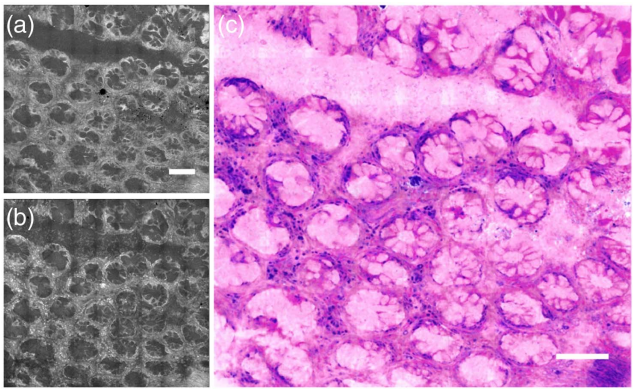

Fig. 4. Virtual-haematoxylin-and-eosin (H&E) image: an image was generated that resembles conventional H&E stained tissue sections using only two coregistered SRS images at 2850 cm^{-1} and 2930 cm^{-1}. Individual nuclei are readily identified as pseudo H-stained blue dots. (a) SRS raw image at 2850 cm^{-1}. (b) SRS difference image of 2930 cm^{-1} and 2850 cm^{-1}. (c) Composite image of (a) and (b). Scale bar equals 100 μm. Image parameters: pixel dwell time = 240 μs, $f_1 = 19.9$ MHz, $f_2 = 20.0$ MHz; resolution = 1800 × 1600; total image acquisition time = 12 min.

Fig. 3(b) displays the distribution of retinol without any observable crosstalk of channels.

Concerning its scalability the frequency bandpass of the lock-in amplifier ascends inverse with the acquisition time. As the pixel dwell time for typical SRS imaging ranges between 10–1000 μs the corresponding cross-talk free modulation frequency intervals have to be selected to be larger than 100–1 kHz, respectively. Using state-of-the-art multichannel modulators at center frequencies around several tenths of megahertz, almost no limitations are set. Scaling of the presented approach from dual-channel to a multichannel configuration is, therefore, a question of the sample's damage threshold and remains an engineering task to provide further laser sources at different relevant Raman resonances.

To establish further the relevance of the implementation of dual-channel SRS the ability to acquire virtual-H&E images is demonstrated. The SRS images at 2850 cm^{-1} as well as the difference of 2930 cm^{-1} and 2850 cm^{-1} of a human 15 μm thick colon section are displayed in Figs. 4(a) and 4(b), respectively. To generate the virtual-H&E image the difference SRS image is attributed to the purple channel that corresponds to the haematoxylin stain outlining the location of nuclei. This image is further superimposed by the original SRS images at 2850 cm^{-1} in rose-colored mimicking eosin to highlight the cytoplasm. The resulting virtual-H&E image enables various pathologically relevant features to be extracted such as the nuclei/cytoplasm ratio, nuclei size, or the anisotropy of the cell and colon's crypt shape. Accordingly, trained pathologist may use these types images for colon cancer detection or assignment of histopathological indexes such as the activity, chronicity, and architecture in inflammatory bowel diseases, e.g., Crohn's disease or ulcerative colitis [21].

In conclusion, we demonstrated a simple method for the implementation of a dual-channel SRS setup requiring a single detector that is connected to two independent lock-in units. Superior to comparable methods the dual-frequency, dual-OPO approach is not restricted to a limited bandwidth, e.g., the CH-stretching range, nor does it suffer from scattering artifacts or larger power losses while converting femtosecond pulses to picosecond pulses. Further, no excitation power is lost as in broadband excitation approaches while addressing silent Raman shift areas. The latter reduces the maximum obtainable signal and, consequently, compromises critically the signal to noise ratio (S/N) as an improvement of the S/N by a factor of n for a shot noise limited system, requiring n^2 times longer integration time. Previous studies relying on coherent Raman techniques that combined sequentially Raman fingerprint information with contrast arising from the CH-stretching vibrations [22] may be revised and extended as a major benefit of the presented dual-frequency implementation. Furthermore, the images obtained can be used to correct for SRS artifacts when targeting simultaneously a resonant and a nonresonant signal such as deuterated carbon (CD) bond imaging [23] or be employed to generate perfectly coregistered virtual-H&E images as shown in Fig. 4. The latter may serve as a vantage point for a following human evaluation or an automatic prediction of diagnosis.

Funding. Conseil National de la Recherche Scientifique (CNRS); Institut National de la santé et de la recherche médicale (Inserm) (PC201508); Agence Nationale de la Recherche (ANR) (ANR-11-INSB-0006, ANR-10-INSB-04-01); Aix-Marseille Université (AMU) (noANR-11-IDEX-0001-02).

REFERENCES

1. J.-X. Cheng and X. S. Xie, eds., *Coherent Raman Scattering Microscopy*, Series in Cellular and Clinical Imaging (CRC Press, 2016).
2. D. A. Orringer, B. Pandian, Y. S. Niknafs, T. C. Hollon, J. Boyle, S. Lewis, M. Garrard, S. L. Hervey-Jumper, H. J. L. Garton, C. O. Maher, J. A. Heth, O. Sagher, D. A. Wilkinson, M. Snuderl, S. Venneti, S. H. Ramkissoon, K. A. McFadden, A. Fisher-Hubbard, A. P. Lieberman, T. D. Johnson, X. S. Xie, J. K. Trautman, C. W. Freudiger, and S. Camelo-Piragua, Nat. Biomed. Eng. **1**, 0027 (2017).
3. T. W. Bocklitz, F. S. Salah, N. Vogler, S. Heuke, O. Chernavskaia, C. Schmidt, M. J. Waldner, F. R. Greten, R. Bräuer, M. Schmitt, A. Stallmach, I. Petersen, and J. Popp, BMC Cancer **16**, 534 (2016).
4. Y. Ozeki, W. Umemura, Y. Otsuka, S. Satoh, H. Hashimoto, K. Sumimura, N. Nishizawa, K. Fukui, and K. Itoh, Nat. Photonics **6**, 845 (2012).
5. P. Berto, E. R. Andresen, and H. Rigneault, Phys. Rev. Lett. **112**, 053905 (2014).
6. E. Ploetz, S. Laimgruber, S. Berner, W. Zinth, and P. Gilch, Appl. Phys. B **87**, 389 (2007).
7. K. Seto, Y. Okuda, E. Tokunaga, and T. Kobayashi, Rev. Sci. Instrum. **84**, 083705 (2013).
8. J. Réhault, F. Crisafi, V. Kumar, G. Ciardi, M. Marangoni, G. Cerullo, and D. Polli, Opt. Express **23**, 25235 (2015).
9. D. Zhang, M. N. Slipchenko, D. E. Leaird, A. M. Weiner, and J.-X. Cheng, Opt. Express **21**, 13864 (2013).
10. E. R. Andresen, P. Berto, and H. Rigneault, Opt. Lett. **36**, 2387 (2011).
11. R. He, Y. Xu, L. Zhang, S. Ma, X. Wang, D. Ye, and M. Ji, Optica **4**, 44 (2017).
12. M. S. Alshaykh, C.-S. Liao, O. E. Sandoval, G. Gitzinger, N. Forget, D. E. Leaird, J.-X. Cheng, and A. M. Weiner, Opt. Lett. **42**, 1548 (2017).
13. X. Audier, N. Balla, and H. Rigneault, Opt. Lett. **42**, 294 (2017).
14. D. Fu, F.-K. Lu, X. Zhang, C. Freudiger, D. R. Pernik, G. Holtom, and X. S. Xie, J. Am. Chem. Soc. **134**, 3623 (2012).
15. C.-S. Liao, P. Wang, P. Wang, J. Li, H. J. Lee, G. Eakins, and J.-X. Cheng, Sci. Adv. **1**, e1500738 (2015).

16. S. Heuke, O. Chernavskaia, T. Bocklitz, F. B. Legesse, T. Meyer, D. Akimov, O. Dirsch, G. Ernst, F. von Eggeling, I. Petersen, O. Guntinas-Lichius, M. Schmitt, and J. Popp, Head Neck **38**, 1545 (2016).
17. X. Chen, P. Gasecka, F. Formanek, J.-B. Galey, and H. Rigneault, Br. J. Dermatol. **174**, 803 (2016).
18. S. Brustlein, P. Ferrand, N. Walther, S. Brasselet, C. Billaudeau, D. Marguet, and H. Rigneault, J. Biomed. Opt. **16**, 021106 (2011).
19. W. G. Fateley, G. L. Carlson, and F. E. Dickson, Appl. Spectrosc. **22**, 650 (1968).
20. K. M. Marzec, K. Kochan, A. Fedorowicz, A. Jasztal, K. Chruszcz-Lipska, J. C. Dobrowolski, S. Chlopicki, and M. Baranska, Analyst **140**, 2171 (2015).
21. O. Chernavskaia, S. Heuke, M. Vieth, O. Friedrich, S. Schürmann, R. Atreya, A. Stallmach, M. F. Neurath, M. Waldner, I. Petersen, M. Schmitt, T. Bocklitz, and J. Popp, Sci. Rep. **6**, 29239 (2016).
22. F. B. Legesse, S. Heuke, K. Galler, P. Hoffmann, M. Schmitt, U. Neugebauer, M. Bauer, and J. Popp, Chem. Phys. Chem. **17**, 4043 (2016).
23. X. Chen, S. Grégoire, F. Formanek, J.-B. Galey, and H. Rigneault, J. Control. Release **200**, 78 (2015).